



Cite this: *RSC Adv.*, 2020, 10, 25073

BiOCl/WS₂ hybrid nanosheet (2D/2D) heterojunctions for visible-light-driven photocatalytic degradation of organic/inorganic water pollutants

Waseem Ashraf,^a Shikha Bansal,^a Vikrant Singh,^b Sanmitra Barman^b and Manika Khanuja ^{*a}

This report presents the superior visible-light-driven photocatalytic response of novel 2D/2D BiOCl/WS₂ (BW_x) hybrid nanosheet heterojunctions prepared by a simple solution based sonochemical technique. These BW_x hybrid nanosheets are composed of 2D transition metal dichalcogenide material WS₂ and BiOCl nanosheets. The comparative study of photocatalytic activity of BiOCl and BiOCl/WS₂ hybrid nanosheets is carried out *via* photodegradation of Malachite Green (MG) and photoreduction of heavy metal ion Cr(vi) under visible light irradiation. The quantum efficiency of the samples is estimated in terms of the incident photon to electron conversion efficiency (IPCE) measurements. Nearly 98.4% of the MG degradation was achieved over BiOCl/WS₂ (2%) photocatalyst in 45 min of irradiation. BiOCl/WS₂ (2%) hybrid nanosheet catalyst showed the highest external quantum efficiency (EQE) in both the UV and visible regimes. This accomplishment demonstrated the promise of commercial application of the 2D/2D BiOCl/WS₂ (2%) hybrid nanosheet photocatalyst.

Received 31st March 2020
Accepted 15th June 2020

DOI: 10.1039/d0ra02916e

rsc.li/rsc-advances

1. Introduction

The crises of global energy and increasing pollution in the environment are the two major concerns that the whole world would be looking for immediate yet sustainable solutions.^{1,2} The utilization of non-conventional sources of energy such as wind and visible light can be the most suitable remediation for the energy crisis and pollution. Among the sources of different renewable energy, using solar energy for the degradation of pollutants is of high demand.^{3–5} Since the first report on TiO₂ catalyzed water splitting under the UV irradiation by Fujishima and Honda,⁶ there has been a plethora of examples of hydrogen gas production *via* water splitting using solar energy and water disinfection by using photocatalytic degradation of water pollutants.^{7–14} The photocatalytic degradation of water pollutants is a very promising technology being an eco-friendly, low cost technique and having a lack of any consequential contamination.^{15–17} A large variety of semiconductor nano-heterostructures have been proposed and fabricated to date that contribute to the advancement of photocatalytic conversion technology.^{18–21} However, making a photocatalyst with high

efficiency, low recombination rate and maximum visible light absorption in the full spectral range is still a challenge.

The most commonly used organic dyes in the textile, pharmaceutical, and cosmetic industries are Methyl orange; Malachite green; Rhodamine B; Methylene blue; Congo red, *etc.* When these organic dyes are discharged into water resources, they can be very harmful.^{22–25} Malachite Green (MG), a water-soluble cationic dye used as an antifungal, antimicrobial and a topical antiseptic in aquaculture since 1930,^{26,27} has a structure similar to carcinogenic triphenylmethane dyes. Besides, the effluent containing Cr(vi) ions, the inorganic heavy metal water pollutant, is very toxic and detrimental to the environment.²⁸ Various common techniques are being used to take out Cr(vi) from water *viz.* ultra-filtration, adsorption, reverse osmosis, *etc.*²⁹ However, these methods have high power consumption and high operating cost. In an alternate approach for the removal of organic/inorganic pollutants of water, the development of an efficient photocatalyst that can work in the entire solar spectrum (that reaches our earth's surface), is of utmost priority because of low operating cost.³⁰ Many materials, like α -Ga₂O₃, activated carbon from rice husk, and *Cocos nucifera* has been investigated and used as photocatalysts by researchers.³¹ However, the degradation efficiency of these materials was found to be less than 65% even after using a comparatively higher dosage of catalyst. This lead the researchers to find a new class of materials that include, Fe doped TiO₂, Ag₃PO₄ modified by MWCNT's, UiO-66-NH₂(Zr/Hf)

^aCentre for Nanoscience and Nanotechnology, Jamia Millia Islamia, New Delhi-110025, India. E-mail: manikakhanuja@gmail.com

^bCenter for Advanced Materials and Devices, BML Munjal University, Haryana-122413, India



and z-scheme based photocatalysts which increased the degradation efficiency to about 85%, but with high photocatalyst dosage. Also, the synthesis of this class of materials is complicated in comparison to the photocatalyst synthesized in the present work.^{29,32}

In the last few years, bismuth-based semiconductors *viz.* bismuth oxyhalides have attracted many researchers due to their large optical and chemical stability, non-toxicity, cost-effectiveness, and potential application in photocatalytic energy conversion and water disinfection.^{30,33} One of the oxyhalides of bismuth, BiOCl, a ternary semiconductor (V–VII), has a wide bandgap ranging from ~3.17–3.54 eV (ref. 34) possessing a layer-type structure consisting of [Bi₂O₂]²⁺ and Cl[–] located in between the layers.³⁵ This type of layered geometry facilitates the generation of an internal electric field useful for escalating the separation of the photo-induced electron–hole pairs leading to photoactivity.³⁶ BiOCl generally gives higher photocatalytic response with UV-light irradiation in comparison to TiO₂, due to its layer-type geometry.³⁷ Besides, the wide bandgap of BiOCl degrades the photocatalytic activity in the visible-light regime. Hence, the extension of the photocatalytic properties of BiOCl nanostructures in the visible region has become a topic of interest for many researchers. Various methods, like dehalogenation, surface functionalization, photosensitization effect, metal/non-metal doping, and heterojunction constructions are being applied to modify BiOCl for the enhancement of absorption of light in the UV-visible regime.^{38–43} Among these, methods, making a heterojunction composed of BiOCl and another semiconductor with narrow bandgap lying in the visible regime having suitably positioned valence band maxima and conduction band minima, can be promising in the enhancement of visible-light harvesting, decreasing the electron–hole recombination rate and increasing the lifespan of the charge carriers. Numerous combinations of heterojunction systems, *e.g.* Bi₂WO₆/BiOCl, Bi₂S₃/BiOCl, g-C₃N₄/BiOCl, BiOCl/RGO, BiOI/BiOCl, CdS/BiOCl, WO₃/BiOCl, BiVO₄/BiOCl, NaBiO₃/BiOCl, BiOCl/TiO₂, *etc.*^{44–49} have been investigated by many researchers. It has been found that these heterojunctions show enhanced photocatalytic performance in comparison to their counterparts. However, there is only a single report present to date on the BiOCl/WS₂ heterostructure system showing the enhanced photocatalytic response in degrading complex organic dyes.⁴⁹

Tungsten disulfide (WS₂) belongs to the family of 2D transition metal dichalcogenides (TMDs). It possesses a direct bandgap in the range ~1.35–2 eV that leads to the absorption of light to 910 nm.⁵⁰ So, the combination of BiOCl and WS₂ nanosheets can significantly improve the spectrum absorption efficiency *via* bandgap modification and efficient charge transfer. Hence, a detailed investigation of the BiOCl/WS₂ heterostructure system is important for the water remediation by photocatalytic degradation of the pollutants.

In the present study, the 2D/2D nanostructure composite of WS₂ nanosheets and BiOCl nanosheets were prepared by using a simple solution based sonochemical technique. The study of photodegradation of Malachite Green (MG) and the photoreduction of a very toxic heavy metal ion Cr(vi)) was carried out

under visible light irradiation using BiOCl/WS₂ hybrid nanosheets. The photocatalytic response of BiOCl/WS₂ was significantly affected by the amount of WS₂ incorporated. The combination of BiOCl and WS₂ nanosheets resulted in the enhancement of the charge carriers' transfer rate, resulting in better photocatalytic activity.

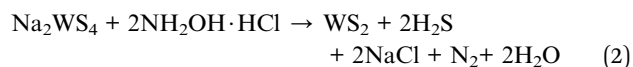
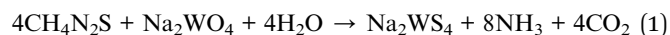
2. Experimental details

2.1 Reagents and materials

In the present work, all the chemicals used were of analytical grade unless otherwise mentioned and were used as they were bought from the supplier without any additional purification. Sodium tungstate dihydrate (Na₂WO₄·2H₂O, 96%) and thiourea (CH₄N₂S) were bought from the Thermo Fischer Scientific India (P) Ltd., Mumbai, India. Hydroxylamine hydrochloride (NH₂·OH·HCl, 98%) and *N*-cetyl-*N,N,N*-trimethyl ammonium bromide (CTAB, 98%) were purchased from Central Drug House (P) Ltd., New Delhi, India. The pH value of the solution was maintained using buffer capsules (Merck, India). Potassium dichromate (K₂Cr₂O₇, Merck, India, 99.99%) was used as a source of chromium. Bismuth nitrate pentahydrate (reagent grade, Bi(NO₃)₃·5H₂O, 98%), HCl (37%), NaOH (≥97%, pellets), *n*-propanol (99.7%), and ethanol (99.9%, AR grade) were sourced from Sigma Aldrich, India.

2.2 Synthesis of WS₂ nanosheets

The solution was prepared by mixing 0.005 M sodium tungstate, 0.02 M thiourea, and 0.01 M hydroxylamine hydrochloride in 30 ml DI water. In this solution, 0.24 g CTAB was added and stirred constantly for 60 min. The measured pH value of the white-colored precipitate thus formed was 6.15. The solution was then poured into a teflon lined autoclave. For 24 h the autoclave was kept in a furnace at a temperature of 180 °C. After 24 h the autoclave was taken out from the furnace and kept at room temperature for natural cooling. After natural cooling, the solution was filtered. The solid content thus recovered was washed with DI water and ethanol. Then the content was dried at a temperature of 30 °C inside the furnace for 4 h.⁵¹ The chemical reactions involved in the synthesis of WS₂ nanosheets are as follows:



2.3 Synthesis of WS₂ nanosheets and BiOCl nanosheets hybrid

A solution of *n*-propanol (10 ml) and hydrochloric acid (2 M, 25 ml) was prepared in 20 ml DI water. In this solution, 1.86 g Bi(NO₃)₃·5H₂O and a measured amount of WS₂ nanosheets were added. The whole solution thus formed was then ultrasonicated for 30 min to get a uniform suspension. The



suspension thus formed was turned white steadily after adding ~10 ml of 4 M NaOH aqueous solution, drop by drop. The pH value of the mixture was found to be 8.0. The suspension was mixed with stirrer for 30 min and then kept as it is for 6 h. The formed resultant precipitates formed were centrifuged and washed using ethanol and DI water thoroughly. At last, the precipitates were dried at 100 °C for 12 h to achieve BiOCl/WS₂ hybrid nanosheets (Fig. 1).

A series of BiOCl/WS₂ hybrid nanosheets by varying the wt% of WS₂ from 0% to 5% were synthesized and denoted as BW_X hybrid nanosheets, where X denotes the weight percentage of WS₂ nanosheets to BiOCl. Pure BiOCl nanosheets (BW₀) were synthesized under similar conditions without the addition of WS₂ nanosheets.

2.4 Characterization

FESEM (Field Emission Scanning Electron Microscopy) study was carried out using Zeiss, Sigma Field Emission Scanning Electron Microscope, to investigate the morphology of the samples. EDX (Energy Dispersive X-ray) spectra taken from FESEM were used for composition analysis. Crystal structure and phase identification studies were carried out through X-ray diffractogram (XRD Smart Lab Guidance, Rigaku) were recorded by using Cu K_α source with wavelength, $\lambda = 1.5418 \text{ \AA}$. The Raman scattering measurements were conducted using Alpha 300 RAS TS-150 Witec Confocal Raman Microprobe equipped with 365 nm and 532 nm argon-ion lasers. The absorption of light in 300–800 nm range was investigated by UV-vis diffuse reflectance spectroscopy (UV-vis Cary Series, Agilent Technologies). Photocatalytic activity of the BW_X hybrid nanosheets for MG degradation and highly toxic Cr(vi) ion reduction was analyzed using the UV-vis spectrometer (UV-vis Cary Series, Agilent Technologies). Fourier transform infrared spectroscopy (FTIR) (Vertex 70V, Bruker) was used to study the functional groups and bond structure. The lifetime of charge carriers was

evaluated by using the Time-Correlated Single-Photon Counting (TCSPC) (Horiba DeltaFlex-01-DD) measurement spectrometer at an excitonic emission wavelength of 280 nm with typical short optical pulses from <100 ps optical FWHM, spectral FWHM < 15 nm in pulsed mode, 100 MHz maximum repetition rate, and with an instrument response function of ~200 ps. The emission decays were deconvolved with IRF using EZ time software. The double-exponential kinetics model was used to fit the decay curves of the samples and the fitting was done in the best fitness limits, with χ^2 in the range 1–1.2. The relationship between the photoactivity improvement and the wavelength of the incident light, and the external quantum efficiency of the samples were investigated by using Incident Photon to Converted Electron (IPCE) studies. For IPCE measurements, 100 mg of photocatalyst was compressed under a pelletizer using a 10 mm stainless steel die and the applied force was 50 kN. The thin pellet with 10 mm diameter was annealed for 2 hours at a temperature of 50 °C. For electrode preparation, silver paste was applied to one of the faces of the pellet and a thin copper wire was placed on the silver pasted face and again the silver paste was applied to the copper wire at the contact point as well to make the ohmic contact. The silver paste was allowed to dry for at least 1 hour to make sure that the proper contact is established. The other end of the wire was inserted through thin hollow glass pipe with 2 mm diameter and 3-inch height. One end of the pipe was kept close to the edge of the pellet and at this end, resin was applied to the copper wire, silver pasted face, edge of pellet and thin pipe in such a way that only the bare side of pellet could come in contact with electrolyte when dipped in it. In this case, 1 molar sodium sulphate (Na₂SO₄) was used as an electrolyte. After the whole setup was kept in place, a linear sweep voltammetry was performed with the help of Autolab PGSTAT302N potentiostat and simultaneously the bare face of the sample was illuminated with the help of monochromator which was controlled by lab view programme to automatically select a particular wavelength (in the range of 200–700 nm) for measurement of electrode current as a function of wavelength.

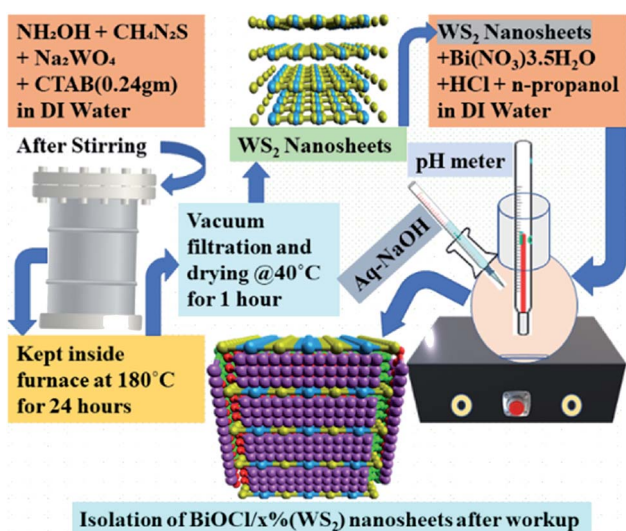


Fig. 1 Schematic diagram of the synthesis of BW_X (X varies from 0% to 5%) hybrid nanosheets.

2.5 Photocatalytic experiment

As-synthesized samples were investigated for their photocatalytic properties by Malachite Green (MG) degradation under visible light. A green-colored solution was prepared by mixing 1 mg of MG in 100 ml of DI water. The solution was then kept in the dark for half an hour. After half an hour, 50 mg BW_X (X = 0%, 2%, and 4%) was added in the solution. Again, the solution was kept in the dark for half an hour. Then, the solution was irradiated in visible light by using xenon arc lamp with a power of 100 mW cm⁻² with AM 1.5 filter. Immediately 1 ml solution was transferred into an eppendorf as the first sample and the subsequent samples were collected each after 15 min for 1.5 h. The collected samples were centrifuged to study the absorption spectra of supernatants. The photocatalytic performance of BW_X hybrid nanosheets was further tested for the Cr(vi) ions photoreduction. A solution of 1 mg of Cr(vi) ions was prepared in 100 ml of DI water. Then 50 mg of the photocatalyst was added in this solution. Taking the first sample at 0 min, 1 ml

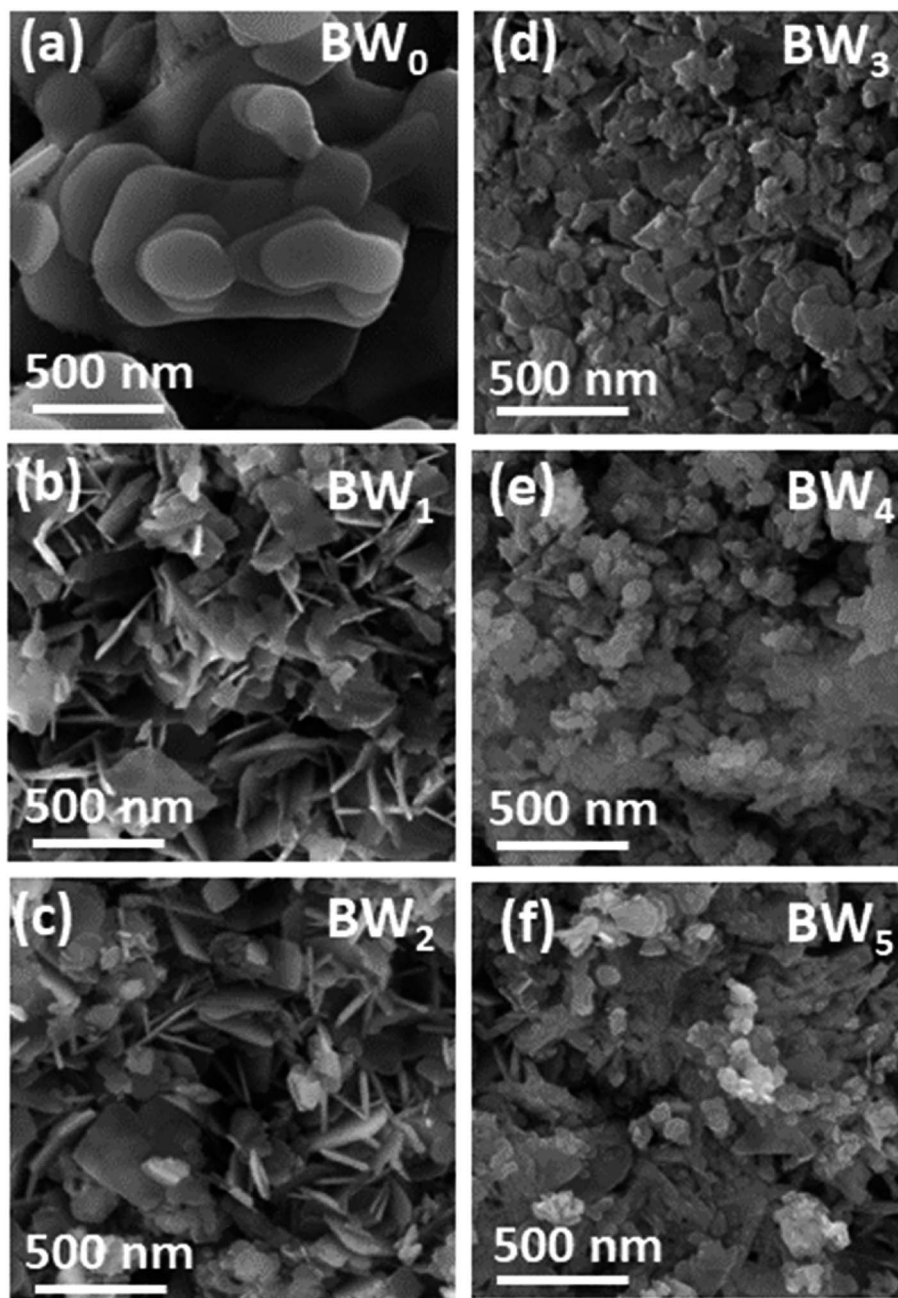


Fig. 2 FESEM images of BW_x hybrid nanosheets where x varies from 0% to 5% prepared by sonochemical method.

sample was taken out of the solution after every 15 min for 3 h. After this, the collected samples were kept for centrifugation and studied for the absorption spectroscopy. The photo-degradation efficiency was calculated by using the formula:

$$\eta = \frac{C_0 - C}{C_0} \times 100\% \quad (3)$$

where C_0 is the initial concentrations of MG/Cr(vi) solutions and C is the concentration at time t , after irradiation.

3. Results and discussion

3.1 Morphology and crystal structure

All the samples' microstructure was studied by FESEM. Morphology in Fig. 2(a) of BW_0 revealed a quite smooth surface with a nanosheet-like structure having round edges and different diameters. The hierarchical plate-like structure for BW_0 was in agreement with the previous report.⁵² Fig. 2(b and f) revealed that the WS_2 incorporation significantly altered the morphology of BiOCl nanosheets in BW_x nanostructures. After the addition of WS_2 , the morphology of the heterojunctions changed to a sheet-like structure with sharp edges. However, the



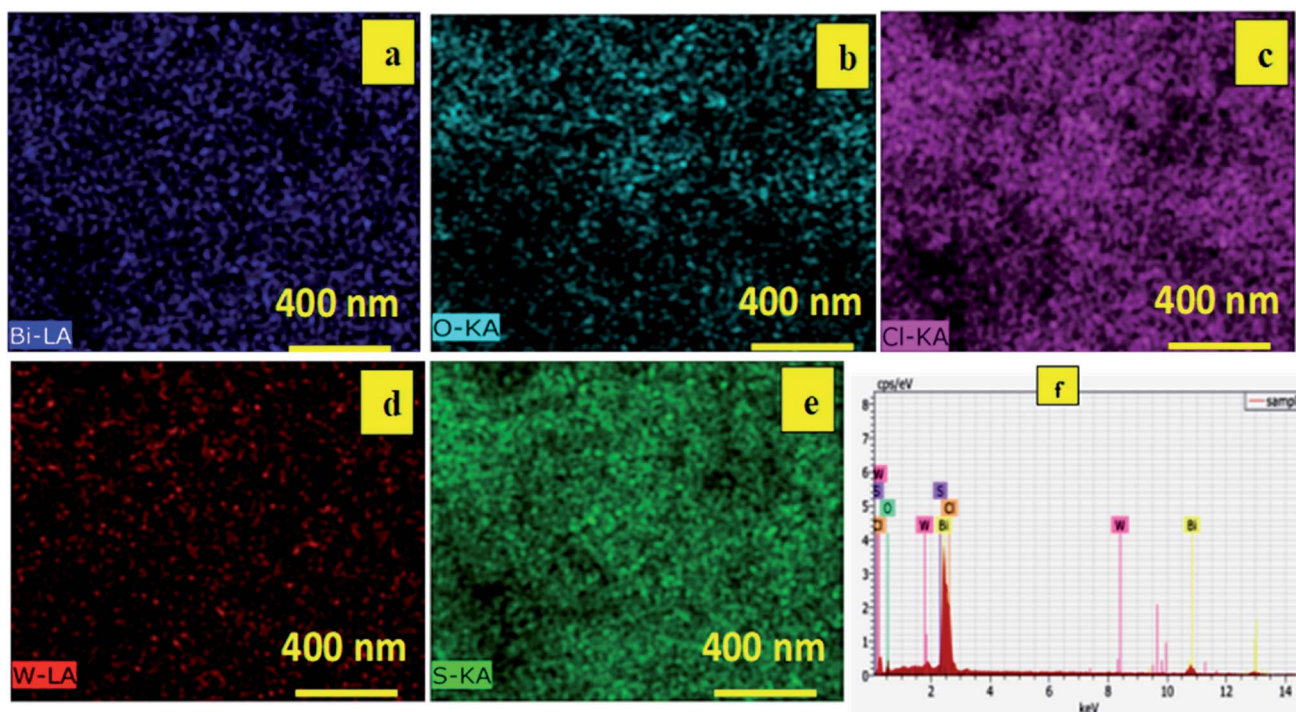


Fig. 3 Elemental mapping of Bi, O, Cl, W and S on the BW_2 nanosheets showing (a) blue, (b) aqua, (c) magenta (d) red (e) green, corresponding to bismuth, oxygen, chlorine, tungsten, and sulphur, respectively and (f) EDX spectra of BW_2 nanosheets.

Table 1 Composition analysis of BW_2 nanosheets

Element	Atomic concentration (%)	Weight concentration (%)
Bi	34	96
O	40	9
Cl	25	12
W	0.6	1.6
S	1.3	0.6

Table 2 Variation of lattice parameters, cell volume (V), and peak intensity ratio (I_{110}/I_{001}) of BW_X hybrid nanosheets where X varies from 0% to 5% with the change in WS_2 content

Samples	a (Å)	c (Å)	V (Å ³)	D_{hkl} (nm)	Intensity ratio (I_{110}/I_{001})
BW_0	3.888	7.358	111.228	118.49	0.41
BW_1	3.888	7.413	112.059	105.41	5.03
BW_2	3.881	7.336	110.496	102.65	3.05
BW_3	3.887	7.374	111.412	98.1	2.13
BW_4	3.882	7.412	111.698	81.49	3.72
BW_5	3.881	7.416	111.701	79.71	2.32

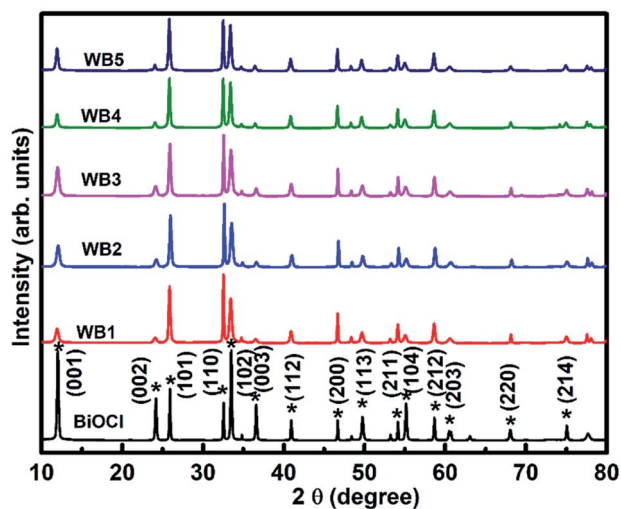


Fig. 4 X-ray diffractograms of BW_X hybrid nanosheets where X varies from 0% to 5% prepared by the sonochemical method.

further increase in WS_2 content ($>3\%$) in $BiOCl$ nanosheets resulted in the agglomeration of the nanosheets. This agglomeration leads to a decrease in active sites for light-harvesting and molecule adsorption.

Energy dispersive X-ray (EDX) was used to study the elemental mapping of BW_2 to confirm the existence of WS_2 in the sample. Fig. 3 depicted that the W and S atoms are evenly spread on the surface of BW_2 hybrid nanosheets, that confirmed the existence of WS_2 . The compositional mapping of BW_2 is given in Table 1, quantitatively.

XRD patterns (Fig. 4) of BW_X (X varies from 0% to 5%) hybrid nanosheets were analyzed to study the crystallographic structure. The 2θ values corresponding to the observed peaks in all the samples were matched with the 2θ values of standard data (JCPDS # 73-2060) of the XRD peaks of pure $BiOCl$. It was found that the as-synthesized samples were pure in-phase and crystallized in the expected tetragonal matlockite structure. In all



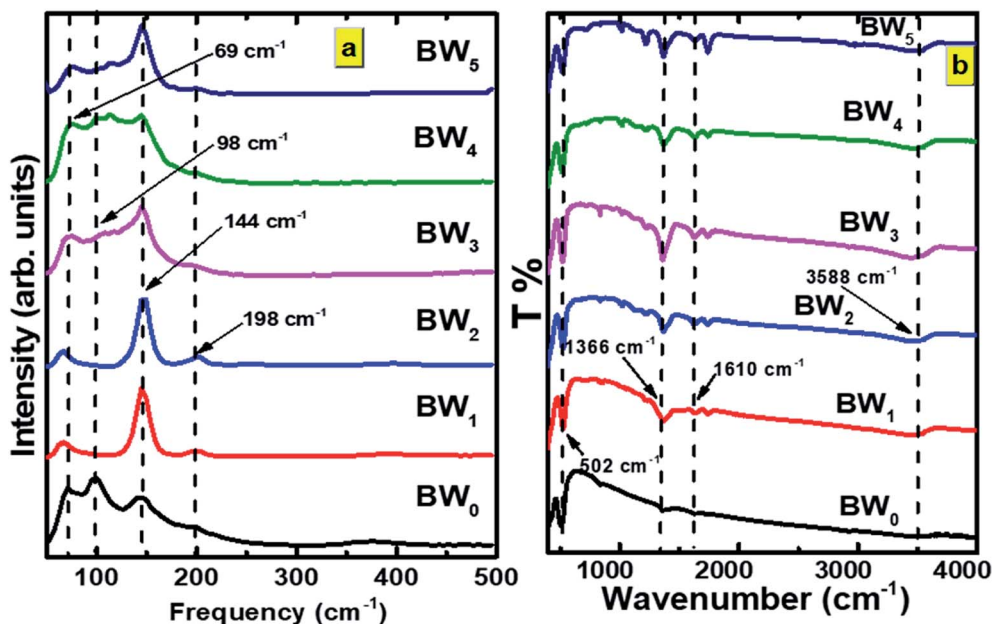


Fig. 5 (a) Raman spectra and (b) FTIR spectra of BW_x hybrid nanosheets where x varies from 0% to 5% prepared by the sonochemical method.

the samples, the XRD peaks displayed the obvious broadening. This broadening of the peaks was attributed to the nanoscale structure of the samples.

The BW_0 nanosheets displayed a pronounced (001) texture. With the addition of WS_2 in $BiOCl$ nanosheets, crystal structure got reoriented from (001) texture to (110) texture followed by (101) texture. The intensity ratios of (110) and (001) peaks for all BW_x hybrid nanosheets are given in Table 2. This reorientation depicts the inhibition of crystal growth along the basal 'ab' plane in the case of BW_x hybrid nanosheets. As per literature, this texture/faceted helps in setting up internal electric fields, that support the electron-hole separation in this type of material.⁵³ It was thus clearly indicated that increasing WS_2 content was accountable for the crystal reorientation in these hybrid

Table 3 Calculated values of the energy band structure parameters of BW_0 , BW_2 , BW_4 hybrid nanosheets, and WS_2 nanosheets

Sample	x (eV)	E_g (eV)	E_{VB} (eV) vs. NHE	E_{CB} (eV) vs. NHE
BW_0	6.36	3.33	3.525	0.195
BW_2	6.36	3.13	3.425	0.295
BW_4	6.36	3.30	3.01	−0.29
W_{NS}	5.66	1.99	2.155	0.165

nanosheets. This kind of crystallographic reorientation was also being reported by Jia *et al.* in $Bi_2S_3/BiOCl$ composites.⁵⁴ The observed change in crystallographic orientation can be attributed to the transition from reduced surface termination to

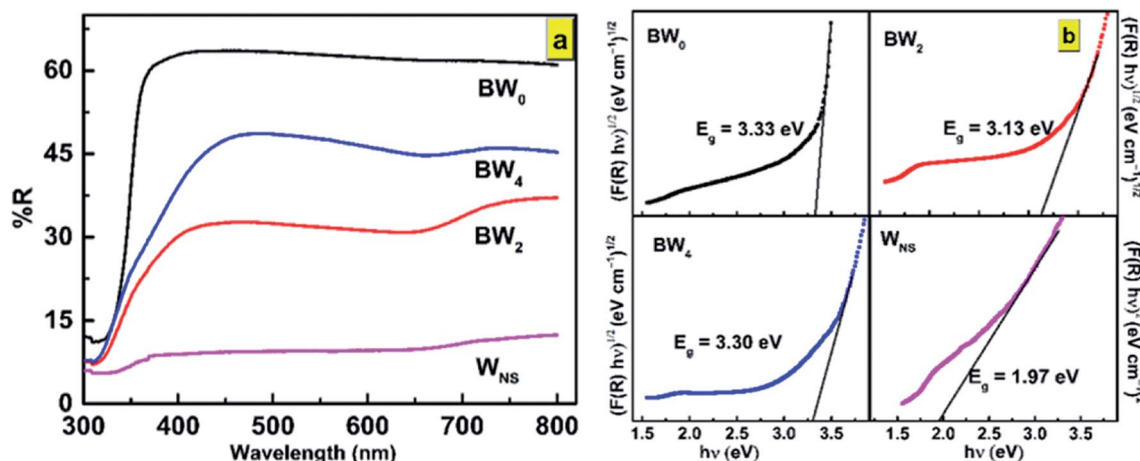


Fig. 6 (a) UV-vis DRS spectra and (b) the plot of $(F(R)h\nu)^{1/2}$ vs. $h\nu$ for determination of bandgap energies of BW_0 , BW_2 , BW_4 , and W_{NS} hybrid nanosheets.



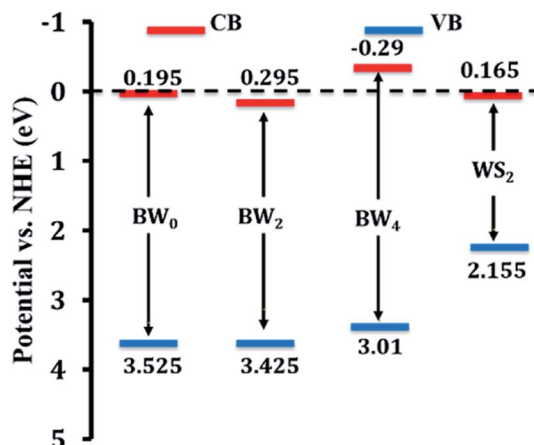


Fig. 7 Schematic illustration of band edge positions of BW_0 , BW_2 , BW_4 hybrid nanosheets and WS_2 nanosheets.

oxidized surface termination and the surface energy stability associated.

The crystallite size of the hybrid nanosheets was evaluated from the Scherrer's formula⁴¹ given as follows:

$$D_{hkl} = \frac{0.9\lambda}{\beta \cos(\theta)} \quad (4)$$

where D_{hkl} (nm) represents the average crystallite size, $\lambda = 0.1540$ nm, is the Cu K_α radiation's wavelength, β (radians) represents the full-width at half-maximum (FWHM) of the peak, and θ is the Bragg's diffraction angle.

It was discovered that the crystallite size decreases from 118.5 to 79.7 nm with the increase in WS_2 content in the $BiOCl$ matrix from 0% to 5% (Table 2). This indicates that the BW_X hybrid nanosheets possessed smaller crystallite sizes with a large surface area. In a tetragonal unit cell, the relationship between interplanar spacing ' d ' of (hkl) planes and the lattice constants ' a ' and ' c ' is given as:

$$\frac{1}{d^2} = \left(\frac{h^2 + k^2}{a^2} \right) + \frac{l^2}{c^2} \quad (5)$$

Table 4 Simulated parameters of eqn (11) and the calculated average lifetime of the BW_X hybrid nanosheets (X varies from 0% to 5%)

Sample	Lifetime (ns)		Relative intensities (%)		Chi-squared
	τ_1	τ_2	f_1	f_2	
BW_0	277.3	6.5	8.2%	91.8%	1.167
BW_1	325.5	8.9	22.4%	78.6%	1.152
BW_2	340.1	9.6	26.1%	73.9%	1.21
BW_3	285.4	7.0	11.6%	88.4%	1.144
BW_4	326.2	9.3	24.2%	75.8%	1.130
BW_5	328.4	9.5	23.9%	76.1%	1.236

(001) and (200) planes were used to calculate the lattice constants all the samples. The calculated lattice parameters were found to agree with the standard values $a = 3.887$ Å, $c = 7.354$ Å, and $V_0 = 111.11$ Å³ corresponding to $BiOCl$. The non-presence of XRD peaks corresponding to WS_2 in the X-ray diffractogram of BW_X is attributed to the presence of WS_2 in a very low amount in the $BiOCl$ precursor. Similar results were reported in the case of $CQDs/BiOI$ and $Co_3O_4/BiOCl$ hybrids.^{55,56}

Information regarding vibration along with the crystal structure and stress state was obtained from the Raman spectra of BW_X hybrid nanosheets (Fig. 5(a)).

Five Raman vibration bands were observed for BW_0 at 69, 98, 144, 198, and 365 cm^{-1} . Peaks at 144 and 198 cm^{-1} were dedicated to the A_{1g} and E_g internal mode of Bi–Cl stretching.³⁷ Peaks at the positions 69 and 98 cm^{-1} were dedicated to the first-order scattering corresponding to E_g and A_{1g} modes of Bi.⁵⁷ This depicts the presence of the unreacted Bi in the $BiOCl$ matrix. It was observed that the BW_1 and BW_2 had a sharp peak at 142 cm^{-1} along with smaller intensity peaks at 67 and 196 cm^{-1} . The high-intensity blue-shifted peak at 142 cm^{-1} followed by the intensity reduction of the other peaks indicated that the addition of WS_2 nanosheets significantly affected the Bi–Cl internal A_{1g} stretching mode. The reduced degrees of freedom along ' a ' and ' b ' axes resulted in restricted stretching in the tetragonal crystal lattice of $BiOCl$.⁵⁸ The blue shift of the

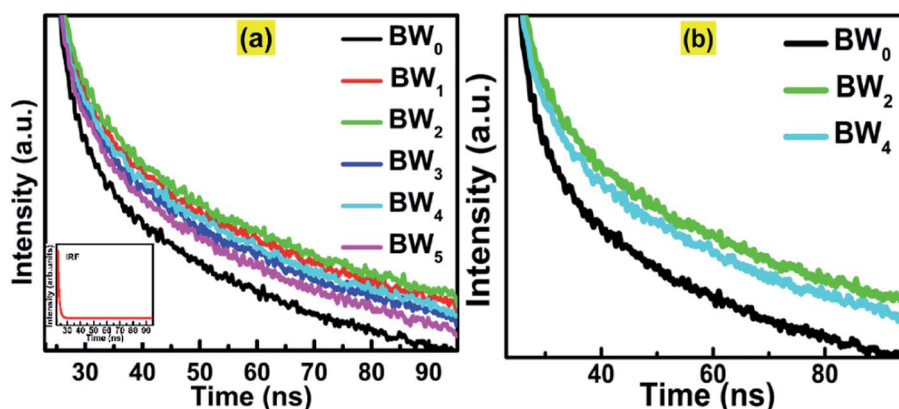


Fig. 8 (a) Time-correlated single-photon counting (TCSPC) spectra of BW_X hybrid nanosheets where X varies from 0% to 5%. Inset shows the IRF data. (b) Magnified TCSPC spectra for BW_0 , BW_2 and BW_4 nanosheets.

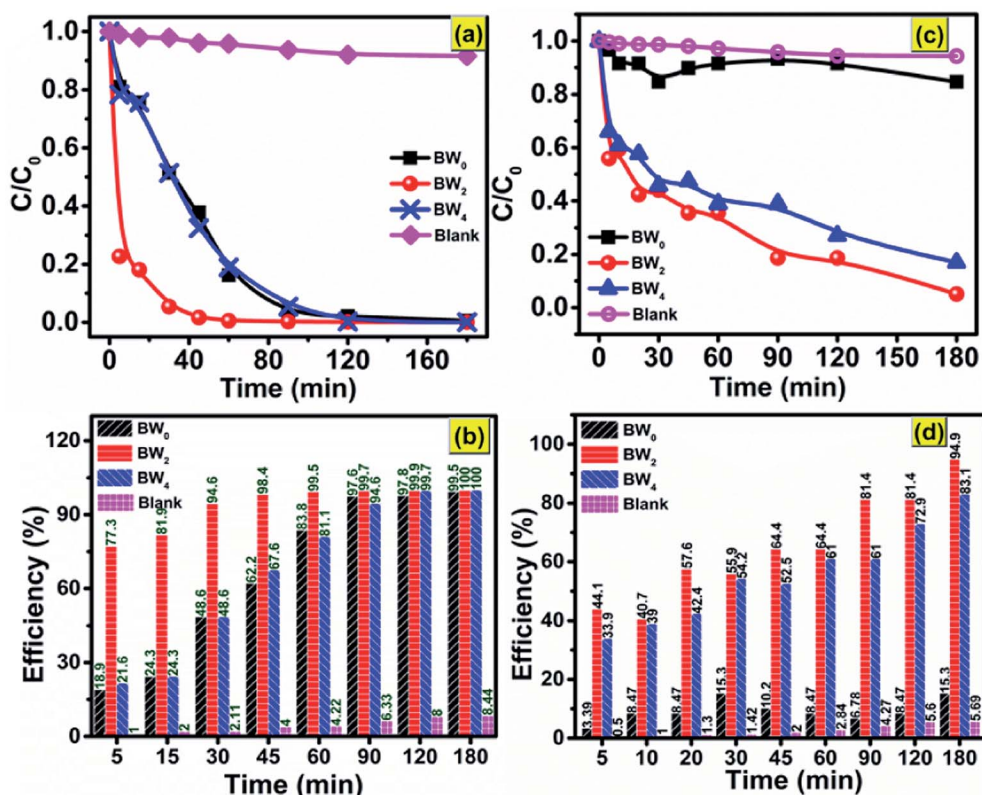


Fig. 9 Photocatalytic degradation of (a) MG dye; (c) $Cr(VI)$ without catalyst and in the presence of BW_0 , BW_2 , and BW_4 under visible light irradiation; photocatalytic efficiency vs. time plot for (b) MG dye and (d) $Cr(VI)$, over BW_0 , BW_2 , and BW_4 hybrid nanosheets.

Raman vibrational peaks in the BW_1 and BW_2 samples evidenced a strong coupling between the $BiOCl$ and WS_2 nanosheets. However, the nature of the Raman spectra for BW_3 , BW_4 , and BW_5 quite similar to that of BW_0 .

FTIR measurements were carried out to further study the phase transformation of $BiOCl$ and interfacial relations between $BiOCl$ and WS_2 . FTIR spectra of BW_x nanostructures are presented in Fig. 5(b). $Bi-O$ stretching vibration at around 502 cm^{-1} was observed in BW_0 which is common in a tetragonal phase $BiOCl$ crystal. $O-H$ stretching frequency was found at 1366 cm^{-1} and 1610 cm^{-1} in BW_0 . A wide hump around

3588 cm^{-1} was dedicated to the presence of H_2O in $BiOCl$.³² In the case of the BW_x hybrid nanosheets, the intensity of $O-H$ stretching vibrations at 1366 cm^{-1} and 1610 cm^{-1} was increased significantly. This implies the presence of a large number of $O-H$ groups at the surface of BW_x hybrid nanosheets. The stretching vibration observed around 671 cm^{-1} and $820-980\text{ cm}^{-1}$ could be allocated to $W-S$ and $S-S$ for the BW_x hybrid nanosheets.⁴² A steady intensification and a shift of the band slightly at $820-980\text{ cm}^{-1}$ in BW_x was due to the strong coupling of $BiOCl$ and WS_2 nanosheets. This strong coupling is vital to escalate the separation and transfer of the charge

Table 5 Previous reports on photocatalytic degradation of MG and $Cr(VI)$ using $BiOCl$ based materials

Catalyst	Dye conc. (mg l^{-1})	Dose (g l^{-1})	Irradiation time (min)	Dyes	Efficiency	Reference
$BiOCl$	25	0.7	120	MG	65%	63
$Sn:BiOCl$	10	—	240	MG	98%	64
$Mn:BiOCl$	25	0.7	480	MG	97%	40
$Bi (Bi_2S_3)/BiOCl$	40	20	40	MG	97.4%	65
$BiOCl_{0.5}Br_{0.5}$	10	—	100	MG	95%	66
$BiOCl/Fe_2O_3$	10	10	300	$Cr(VI)$	50%	67
$BiOCl$	30	—	12	$Cr(VI)$	100%	68
$g-BN/BiOCl$	10	0.8	150	$Cr(VI)$	90%	69
$Ag/BiOCl$	—	—	180	$Cr(VI)$	—	70
$BiOCl/WS_2$	10	0.5	45	MG	98.4%	Present work
	10	0.5	120	$Cr(VI)$	94.9%	

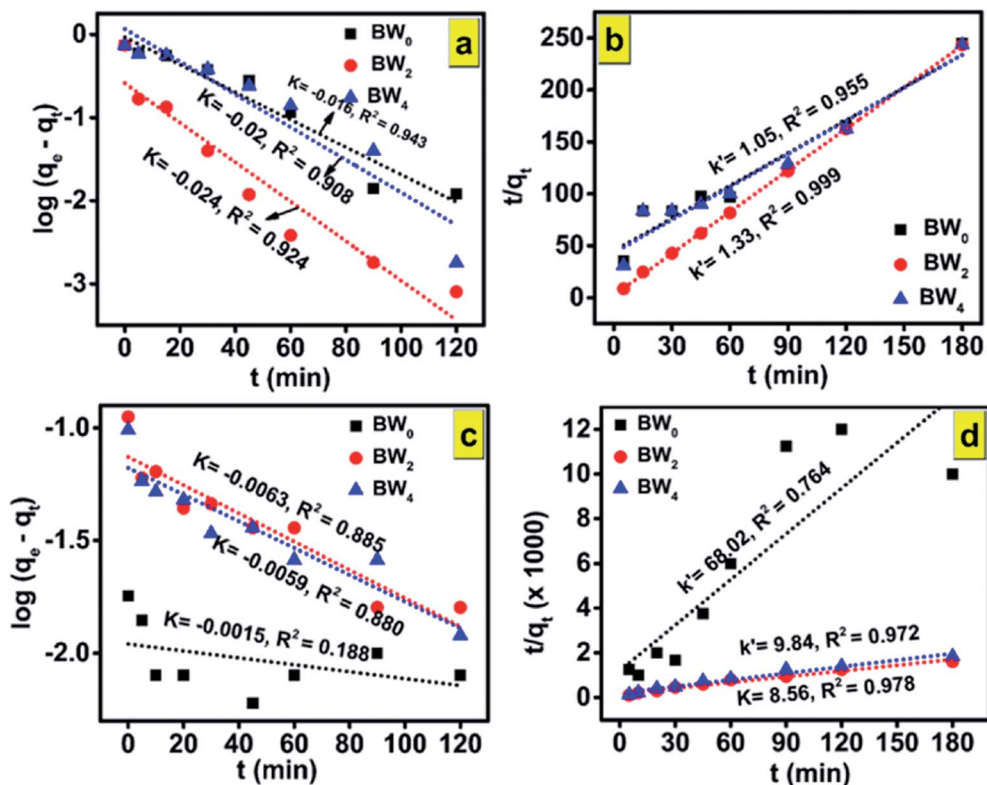


Fig. 10 The adsorption mechanism model of (a and b) organic dye MG and (c and d) heavy metal ion Cr(vi) over BW₀, BW₂, and BW₄ hybrid nanosheets. (a and c) Corresponds to the pseudo-first-order kinetics model; (b and d) corresponds to the pseudo-second-order kinetics model.

carriers and consequently increase the photocatalytic performance of the hybrid nanosheets. The prominent absorption band of W–S was not observed for the hybrid nanosheets, indicating that 2D WS₂ nanosheets are well distributed over the BiOCl matrix.

3.2 Optical properties

From the photocatalysis point of view, one more significant property of BW_x is the absorption of light. The optical properties of BW_x (*X* = 0%, 2%, and 4%), hybrid nanosheets were evaluated by using the UV-vis diffuse reflectance spectroscopy (DRS). The DRS of the pure BiOCl nanosheets is different from the DRS of BW_x hybrid nanosheets (Fig. 6(a)). The BW₀ nanosheets showed a sharp fundamental absorption edge at

~372 nm due to intrinsic bandgap absorption. However, after the incorporation of WS₂ nanosheets into BiOCl nanosheets, the absorption edge of the BW_x hybrid nanosheets was shifted to the lower wavelength. This difference leads to the change in the bandgap of these samples.

3.2.1 Band gap calculations. The bandgap calculation for BW₀, BW₂, and BW₄ hybrid nanosheets and W_{NS} was done by using Kubelka–Munk (K–M) theory from the respective diffuse reflectance spectra (DRS).^{59,60} The relation between the diffuse reflectance (*R*) and the absorbance of the material is given by Kubelka–Munk (K–M) function, *F*(*R*), as follows:

$$F(R) = \frac{K}{S} = \frac{(1 - R)^2}{2R} = \frac{2.303 \times A}{S \times d} \quad (6)$$

Table 6 Parameters of eqn (12) and (13) determined by the adsorption of MG and reduction of Cr(vi) onto the photocatalysts BW₀, BW₂, and BW₄ hybrid nanosheets under visible light irradiation

Sample	Malachite Green (MG)				Chromium ion (Cr(vi))			
	First order		Second order		First order		Second order	
	<i>K</i> (min ^{−1})	<i>R</i> ²	<i>k'</i> (g (mg ^{−1} min ^{−1}))	<i>R</i> ²	<i>K</i> (min ^{−1})	<i>R</i> ²	<i>k'</i> (g (mg ^{−1} min ^{−1}))	<i>R</i> ²
BW ₀	−0.016	0.943	1.05	0.955	−0.002	0.188	68.02	0.764
BW ₂	−0.024	0.924	1.33	0.999	−0.006	0.885	8.56	0.978
BW ₄	−0.02	0.908	1.05	0.955	−0.006	0.880	9.84	0.972



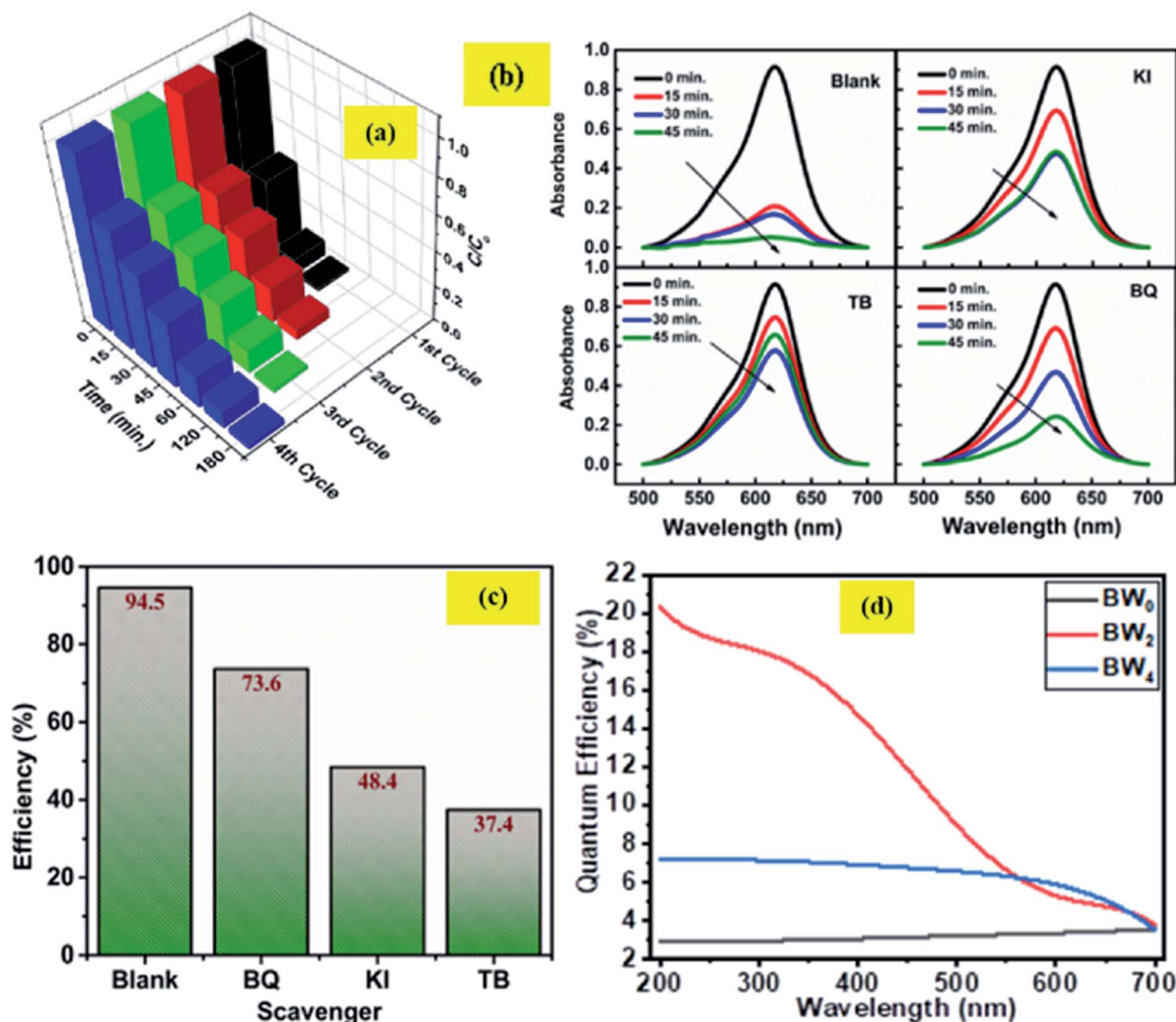


Fig. 11 (a) Cyclic tests of photodegradation of MG on BW₂ hybrid nanosheets. (b) Absorption spectra of MG dye with BW₂ photocatalyst in the presence of various scavengers (BQ, TB, and KI). (c) Effect of various scavengers in the photodegradation process of MG over BW₂ nanosheet hybrid and (d) IPCE spectra of BW₀, BW₂, and BW₄ hybrid nanosheets recorded at 0 V vs. Ag/AgCl in the wavelength range 200–700 nm.

where A is the absorbance of the sample, K is the absorption coefficient, S is the scattering coefficient, and ' d ' is the thickness of the sample. The scattering coefficient, ' S ' accounts for the internal scattering. It depends upon the properties of the material like refractive index and particle size. If we take ' S ' as a constant with respect to wavelength, then $F(R) \propto \alpha$, where ' α ' represents the coefficient of absorption, written as:

$$\alpha = \frac{2.303 \times A}{d} \quad (7)$$

The bandgap energy (E_g) is given by:

$$\alpha h\nu = C(h\nu - E_g)^{\frac{n}{2}} \quad (8)$$

where ' h ' represents the Planck's constant, ' ν ' represents the frequency of light, ' C ' represents the constant of proportionality, and ' E_g ' represents the bandgap energy. ' n ' is an integer and its value is based on nature of the transition occur in

a semiconductor material. n is taken as 4 for an indirect bandgap material and n is taken to be 1 for a direct bandgap material. BiOCl has an indirect bandgap. The value of n was taken to be 4 for BiOCl. However, $n = 1$ for WS₂ as it possesses a direct bandgap transition.

The determination of the bandgap of BW_x (x varies from 0% to 5%) was done by using the graph: $(F(R)h\nu)^{1/2}$ vs. $h\nu$ (Fig. 6(b)). The bandgap energy of the sample is obtained by extrapolating the linear portion of the corresponding $(F(R)h\nu)^{1/2}$ vs. $h\nu$ plots at $(F(R)h\nu)^{1/2} = 0$. The bandgap energy of the BW_x samples is decreased from 3.33 eV to 3.13 eV when the amount of WS₂ is increased from 0% to 4%. The strong coupling between BiOCl and WS₂ nanosheets resulted in a significant bandgap narrowing near the interface. Hence, the sensitivity of the heterostructures towards the visible light is increased which significantly contributes to the visible-light-driven photocatalysis.

The position of E_{VB} , the valence band edge potential and E_{CB} , the conduction band edge potential for BW_X hybrid nanosheets, was calculated by using the Butler and Ginley equation.⁵⁹

$$E_{VB} = X - E_c + 0.5E_g \quad (9)$$

$$E_{CB} = E_{VB} - E_g \quad (10)$$

'X' represents the absolute electronegativity of the semiconductor calculated from the electronegativity of the atoms, it is composed of, ' E_c ' (~ 4.5 eV) represents the free electrons' energy on the hydrogen scale, and ' E_g ' represents the bandgap energy. The calculated E_{VB} and E_{CB} values corresponding to BW_0 , BW_2 , BW_4 , and WS_2 nanosheets are presented in Table 3.

The schematic arrangement of the estimated band edge positions of these samples is presented in Fig. 7.

3.3 Time-correlated single photon counting

The average lifetime of the excitons and dynamics of the photo-induced charge carriers was evaluated by Time-Correlated Single Photon Counting (TCSPC) study (Fig. 8).

The decay curves of the hybrids, BW_X (X varies from 0% to 5%), were simulated by using the double-exponential model.⁶¹

$$I(t) = A_1 \exp\left(-\frac{t}{\tau_1}\right) + A_2 \exp\left(-\frac{t}{\tau_2}\right) \quad (11)$$

where $I(t)$ represents the intensity of photoluminescence, τ_1 and τ_2 represent the decay times corresponding to slower and faster decay processes, respectively, and A_1 and A_2 represent the amplitudes. The inter-band exciton recombination results in a fast PL decay process, however, the slow PL decay process is based on the electron-hole pairs recombine in an indirect mode.⁶²

For pure BiOCl nanosheets, the contribution of the fast decay process with a 6.5 ns lifetime (τ_2), is 91.79% and slow decay process of 277.38 ns (τ_1), contributes only 8.21%. This implies that almost 92% of the excited states are getting deactivated *via* non-radiative path. The incorporation of WS_2 in BiOCl has a significant effect on the dynamics of the charge carriers. 1 wt% addition of WS_2 slows down the decay process by increasing the contribution of τ_1 from 8.2% to 22.36% along

with the increase in both τ_1 and τ_2 at the cost of the contribution of τ_2 . As per Table 4, when the WS_2 content was increased from 1 wt% to 2 wt%, there was a further increase in the contribution of τ_1 from 22% to 26% and the fast, and the slow decay components were lengthened from 8.21 ns to 9.64 ns and 325.49 ns to 340.11 ns. This increment suggests the evolution of new radiative pathways which promote the transfer of a greater number of photoexcited electrons to BiOCl. Similar observations were reported in case of CdS–CdSnO₃ composite.²⁰ Further addition of WS_2 (3 wt%) however shortened the time constant of both the fast and the slow decay components of BiOCl (6.95 ns and 285.41 ns, respectively). This depicted the trapping of charge carrier from WS_2 with the addition of WS_2 content beyond 3 wt% in BiOCl nanosheets. The excess of the charge carrier trapping boosts the electron-hole pair recombination in the nanostructures.⁵³ At relatively higher WS_2 content of 4 wt% and 5 wt%, electrons trapped at BiOCl were such abundant that it helped in the enhancement of recombination rate of the charge carriers across the BiOCl/ WS_2 interface. This outcome depicted that the content of WS_2 beyond a certain optimum value might act as a booster for interfacial electron-hole pairing and the prolonged decay lifetime observed for BW_2 demonstrated the improved charge transfer from WS_2 to BiOCl.

3.4 Photocatalytic response

The as-synthesized BW_0 , BW_2 , and BW_4 hybrid nanosheets were analyzed for their photocatalytic response by Malachite Green (MG) degradation and Cr(vi) ion photoreduction under visible light irradiation. Fig. 9(a) shows the photodegradation of Malachite Green (MG) over BW_0 , BW_2 , and BW_4 hybrid nanosheets. As can be seen in Fig. 9(b), after 30 min irradiation in visible light, $\sim 94.6\%$ of MG was degraded over BW_2 catalysts, whereas only 48.6% of MG was decomposed over BW_0 and BW_4 at the same time. Among all the BW_X (X varies from 0% to 5%) samples, BW_2 showed the highest photocatalytic response towards MG degradation. This was attributed to the incorporated WS_2 nanosheets that helped in structural reorientation and bandgap narrowing. The structure reorientation facilitated the development of internal electric fields that helped in the separation of charge carriers and were beneficial for the charge transfer (revealed by X-ray diffractograms and TCSPC spectra). And bandgap narrowing contributed towards the visible-light-harvesting (confirmed by DRS).

However, too much WS_2 incorporation would result in decreasing the light absorption due to a lowering of the active sites as a result of agglomeration confirmed *via* FESEM images. Hence photocatalytic response got degraded upon increase the WS_2 content beyond 2%. The degradation efficiency for MG reached $\sim 99.5\%$ in 60 min, indicating the high photocatalytic response of BW_2 . The photocatalytic reduction of CrO_3 solution using BW_0 , BW_2 , and BW_4 hybrid nanosheets is shown in Fig. 9(c). It is demonstrated that the BW_2 enabled the photo-reduction of Cr(vi) up to $\sim 95\%$ within 3 h of irradiation (Fig. 9(d)).

To date, only a few reports are present on the photocatalytic degradation of MG and Cr(vi) ions photocatalytic reduction

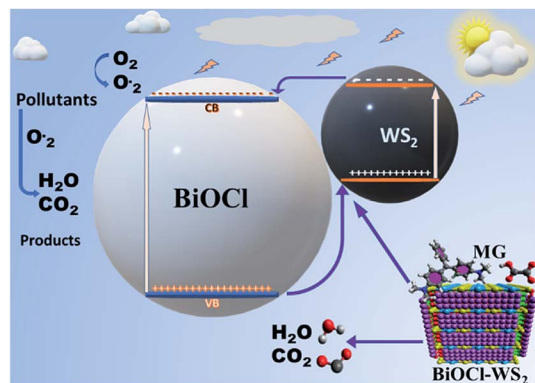


Fig. 12 Schematic diagram of photocatalysis mechanism.



using bismuth oxychloride-based catalysts under visible light irradiation. Some of these previous reports are mentioned in Table 5. Table 5 shows that the BiOCl/WS₂ hybrid nanosheets prepared in the present work are better in the photocatalytic response than the existing bismuth oxychloride-based catalysts. The papers reporting more than 90% degradation efficiency have used a higher photocatalyst dose for a comparatively lower amount of dye to be degraded. The irradiation time taken for the photodegradation is also much higher than the irradiation time taken in the present work. Degradation efficiency ~98.5% in only 45 min and more than 80% in 90 min was achieved in case of 10 mg l⁻¹ of MG and Cr(vi) ions respectively, over only 0.5 g l⁻¹ of BW_x hybrid nanosheets catalysts dosage. This result indicates that the 2D/2D BW_x hybrid nanosheet can be applied as an efficient photocatalyst for the degradation of complex and toxic organic dyes and heavy metal ion pollutants that are extremely hard to degrade.

In general, the experimental data of photocatalytic degradation is simulated by using the pseudo-first and second-order kinetic equations stated as follows:⁷¹

Pseudo-first-order kinetic equation,

$$\log (q_e - q_t) = \log q_e - \frac{Kt}{2.303} \quad (12)$$

Pseudo-second-order kinetic equation,

$$\frac{t}{q_t} = \frac{1}{k'q_e^2} + \frac{t}{q_e} \quad (13)$$

where q_e (mg g⁻¹) represents the amounts of BW_x adsorbed at equilibrium and q_t (mg g⁻¹) represents the amounts of BW_x adsorbed at time t . K (min⁻¹) and k' (g (mg⁻¹ min⁻¹)) represent the rate constants corresponding to pseudo-first and second-order adsorption, respectively.

Fig. 10(a,c) and (b,d) and show the plots of experimental data for MG and Cr(vi), based on eqn (12) and (13), respectively. Table 6 (represents the absorption parameters as per eqn (12) and (13)) shows that the regression coefficient values (R^2) of eqn (12) and (13) are greater than 0.90. Hence, both the models are being followed in case of adsorption of MG over BW_x hybrid nanosheets. Besides, in the case of Cr(vi) ions photoreduction, the R^2 values (>0.90) of eqn (13) are greater than the R^2 values (<0.90) of eqn (12). Hence, we can infer that the adsorption of Cr(vi) ions over BW_x hybrid nanosheets follows only the second-order equation.

Four consecutive tests of photodegradation of MG on BW₂ were run to check the stability of the BW₂ sample. Fig. 11(a) revealed only 10–20% decrease in photocatalytic performance over the consecutive runs. Hence the BW₂ exhibit satisfying chemical stability.

3.5 Active species trapping experiment

Generally, the photo-induced charge carriers *i.e.* electrons and holes are involved in the photocatalytic process. They get involved in the reaction with H₂O/HO⁻ and O₂ and form the superoxide radicals $\cdot\text{OH}$ and $\cdot\text{O}_2^-$ as a product. These active species are fundamentally important in the photocatalytic reactions. In the intention of investigating the active species

involved in the photodegradation process of MG using BW_x hybrid nanosheets, a series of experiments were conducted for trapping the active species in the case of BW₂ nanosheet hybrid. The different scavengers for different active species *viz.* tetra-butanol (TB) for $\cdot\text{OH}$, 1,4-benzoquinone (BQ) for $\cdot\text{O}_2^-$, and potassium iodide (KI) for both $\cdot\text{OH}$ and h^+ were used in the trapping experiments.⁷² Fig. 11(b and c) shows the effect of TB, BQ, and KI on the percentage of photodegradation of MG. The addition of the BQ in MG solution had a little effect on the C/C_0 , indicating that $\cdot\text{O}_2^-$ is the secondary species and not the primary active species during the photocatalytic reaction. On the contrary, the addition of the KI and TB used as $\cdot\text{OH}$ and h^+ scavenger made a considerable impact on the conversion efficiency. The C/C_0 for degradation of MG noticeably decreased after the addition of TB and KI. Therefore, it was established that h^+ and $\cdot\text{OH}$ have a substantial role in MG degradation. These observations propose that photogenerated $\cdot\text{OH}$ is a dominating player in the MG photocatalytic degradation.

3.6 Incident photon to converted electron (IPCE) study

The relationship between the photoactivity improvement and the wavelength of the incident light, and the external quantum efficiency of the samples BW₀, BW₂, and BW₄ were investigated by using Incident Photon to Converted Electron (IPCE) study. In this study, the photocurrent density at each incident wavelength was measured. The IPCE value for a given wavelength was calculated by using the equation

$$\text{EQE} = \frac{J(\lambda)hc}{q_e\lambda P(\lambda)} \times 100\% \quad (14)$$

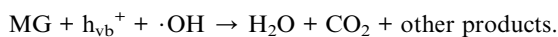
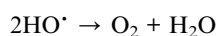
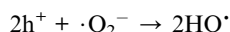
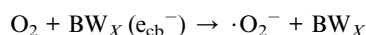
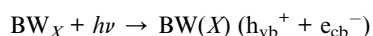
where $J(\lambda)$ is the current density as a function of wavelength in A cm⁻², h (Js) represents the Planck's constant, c (m s⁻¹) is the velocity of light. q_e represents the charge of the electron in C, λ (nm) represents the wavelength of incident light and $P(\lambda)$ (W cm⁻²) represents the intensity of the power that depends on the wavelength of the incident light. Fig. 11(d) displays the IPCE spectra for BW₀, BW₂, and BW₄ hybrid nanosheets. The IPCE values of follows the order: BW₀ < BW₄ < BW₂, in the complete UV-visible spectrum. In particular, the IPCE values of the BW₂ sample at the shorter wavelength region (<400 nm) were 10 times higher (18–20%) than the IPCE values of BW₀ nanosheets. This established that the BW₂ hybrid nanosheet converted the high energy incident photons to electrons well. It is well known that light-harvesting efficiency, charge separation, and collection yields⁷³ play an important role in determining the IPCE value of a sample. Thus, we can further infer that the BW₂ hybrid nanosheets had a larger light-harvesting efficiency and improved charge separation, which was in good agreement with its lower bandgap and slow decay time and better photocatalytic degradation results.

3.7 Photocatalytic mechanism

After being modified with WS₂ nanosheets, the BiOCl/WS₂ nanocomposite showed the higher optical absorption strength in the UV-visible range and larger dye absorption as compared to pure BiOCl nanosheets. The bandgap of BW_x hybrid



nanosheets was also found to be less than the bandgap of pure BiOCl nanosheets. The smaller bandgap of BW_x hybrid nanosheets is responsible for higher visible light absorption. Due to the higher optical absorption of the BW_x hybrid nanosheets, the surface adsorption of the dye was also improved. E_{VB} and E_{CB} corresponding to pure WS₂ nanosheets are about 2.155 and 0.165 eV, respectively. And for pure BiOCl nanosheets, 3.525 and 0.195 eV, respectively. E_{CB} and E_{VB} corresponding to WS₂ are at a higher position than the E_{CB} and E_{VB} corresponding to pure BiOCl, respectively. So, the electrons that are reaching in the conduction band of WS₂ can easily transfer to the conduction band of BiOCl and the holes can easily move from BiOCl to the WS₂ nanosheets (Fig. 12). As depicted by the scavenger test, the photogenerated $\cdot\text{OH}$ radicals play the lead role in the MG photodegradation. The photocatalytic reactions that take place on the surface of BW_x hybrid nanosheets can be described as follows:



Photocatalytic activity is boosted with the increase in the charge carrier separation time, resulting in the hindrance to the charge carrier recombination. The time of the separation of charge carriers decides the number of formation of radicals that take part in the photodegradation of the pollutants.

4. Conclusion

In conclusion, a low-cost sonochemical route has been applied to synthesize a series of 2D/2D hybrid nanosheets of BiOCl/WS₂ having high visible-light absorption. The preparation process was simplified efficiently along with reducing the preparation time. The successful fabrication of 2D/2D hybrid nanosheets of BiOCl/WS₂ is confirmed through the various characterization techniques like XRD, Raman spectroscopy, FTIR spectroscopy, FESEM and EDX. The optical studies including band gap measurement, TCSPC and IPCE confirmed the higher visible light absorption and reduced decay rate of the charge carrier that causes the higher charge transfer rate in the hybrid nanosheets. The as synthesized BW_x hybrid nanosheets exhibited an enhanced photocatalytic response than pure BiOCl nanosheets for MG photodegradation and Cr(vi) ion photoreduction. The BW₂ sample achieved the highest photodegradation rate of more than 99% for MG photodegradation in 60 min under visible light irradiation. The major contributing factors in the enhancement of the photocatalytic performance of BW_x are higher absorption of the visible range, higher rate of charge transfer, larger separation time of photogenerated charge carriers, and high IPCE values in the whole UV-visible spectrum. The photogenerated holes on WS₂ nanosheets that form $\cdot\text{OH}$

radicals, are found to be the primary active species in the photocatalytic process. The combination of high recyclability, high photocatalytic responsivity in visible light, and non-toxicity of the as-synthesized 2D/2D BW_x hybrid nanosheet material pave the way for its usage in photocatalysis, and energy renovation applications. This study provides the scope of incorporation of 2D transition metal dichalcogenides in 2D BiOCl nanosheets to assist bandgap engineering and improve the rate of charge transfer for better photocatalytic activity.

Conflicts of interest

There are no conflicts to declare.

Acknowledgements

This work was supported by Science and Engineering Research Board vide [SERB (No. ECR/2017/001222)] and University Grants Commission vide [UGC (No. F.4-5(201 FRP)/2015(BSR))] to one of the authors (Dr Manika Khanuja). The support is highly acknowledged.

References

- 1 P. R. Gogate and A. B. Pandit, A review of imperative technologies for wastewater treatment I: oxidation technologies at ambient conditions, *Adv. Environ. Res.*, 2004, **8**(3–4), 501–551.
- 2 J. Low, J. Yu and W. Ho, Graphene-Based Photocatalysts for CO₂ Reduction to Solar Fuel, *J. Phys. Chem. Lett.*, 2015, **6**(21), 4244–4251.
- 3 Y. Zhang, G. Zhu, M. Hojamberdiev, J. Gao, J. Hao, J. Zhou and P. Liu, Synergistic effect of oxygen vacancy and nitrogen doping on enhancing the photocatalytic activity of Bi₂O₂CO₃ nanosheets with exposed {001} facets for the degradation of organic pollutants, *Appl. Surf. Sci.*, 2016, **371**, 231–241.
- 4 X. Li, J. Yu and M. Jaroniec, Hierarchical photocatalysts, *Chem. Soc. Rev.*, 2016, **45**(9), 2603–2636.
- 5 S. Wang, X. Yang, X. Zhang, X. Ding, Z. Yang, K. Dai and H. Chen, A plate-on-plate sandwiched Z-scheme heterojunction photocatalyst: BiOBr-Bi₂MoO₆ with enhanced photocatalytic performance, *Appl. Surf. Sci.*, 2017, **391**, 194–201.
- 6 L. Finegold and J. L. Cude, Biological sciences: one and two-dimensional structure of alpha-helix and beta-sheet forms of poly(L-alanine) shown by specific heat measurements at low temperatures (1.5–20 K), *Nature*, 1972, **238**(5358), 38–40.
- 7 M. Wang, Y. S. Chang, C. W. Tsao, M. J. Fang, Y. J. Hsu and K. L. Choy, Enhanced photoelectrochemical hydrogen generation in neutral electrolyte using non-vacuum processed CIGS photocathodes with an earth-abundant cobalt sulfide catalyst, *Chem. Commun.*, 2019, **55**(17), 2465–2468.
- 8 P. Y. Hsieh, Y. H. Chiu, T. H. Lai, M. J. Fang, Y. T. Wang and Y. J. Hsu, TiO₂ nanowire-supported sulfide hybrid



- photocatalysts for durable solar hydrogen production, *ACS Appl. Mater. Interfaces*, 2019, **11**(3), 3006–3015.
- 9 Y. S. Chang, M. Choi, M. Baek, P. Y. Hsieh, K. Yong and Y. J. Hsu, CdS/CdSe co-sensitized brookite H:TiO₂ nanostructures: charge carrier dynamics and photoelectrochemical hydrogen generation, *Appl. Catal., B*, 2018, **225**, 379–385.
 - 10 H. Mittal and M. Khanuja, Nanosheets- and nanourchins-like nanostructures of MoSe₂ for photocatalytic water purification: kinetics and reusability study, *Environ. Sci. Pollut. Res.*, 2019, DOI: 10.1007/s11356-019-06275-8.
 - 11 Y. H. Chiu and Y. J. Hsu, Au@Cu₂S₄ yolk@shell nanocrystal-decorated TiO₂ nanowires as an all-day-active photocatalyst for environmental purification, *Nano Energy*, 2017, **31**, 286–295.
 - 12 I. Siddiqui, H. Mittal, V. K. Kohli, P. Gautam, M. Ali and M. Khanuja, Hydrothermally synthesized micron-sized, broom-shaped MoSe₂ nanostructures for superior photocatalytic water purification, *Mater. Res. Express*, 2018, **5**(12), 11–14.
 - 13 C. N. Van, T. H. Do, J. W. Chen, W. Y. Tzeng, K. A. Tsai, H. Song, H. J. Liu, Y. C. Lin, Y. C. Chen, C. L. Wu, C. W. Luo, W. C. Chou, R. Huang, Y. J. Hsu and Y. H. Chu, WO₃ mesocrystal-assisted photoelectrochemical activity of BiVO₄, *NPG Asia Mater.*, 2017, **9**, 357.
 - 14 T. H. Do, C. N. Van, K. A. Tsai, L. T. Quynh, J. W. Chen, Y. C. Lin, Y. C. Chen, W. C. Chou, C. L. Wu, Y. J. Hsu and Y. H. Chu, Superior photoelectrochemical activity of self-assembled NiWO₄-WO₃ heteroepitaxy, *Nano Energy*, 2016, **23**, 153–160.
 - 15 Y. H. Chiu, T. F. M. Chang, C. Y. Chen, M. Sone and Y. J. Hsu, Mechanistic insights into photodegradation of organic dyes using heterostructure photocatalysts, *Catalysts*, 2019, **9**(5), 430.
 - 16 Y. H. Chiu, T. H. Lai, M. Y. Kuo, P. Y. Hsieh and Y. J. Hsu, Photoelectrochemical cells for solar hydrogen production: challenges and opportunities, *APL Mater.*, 2019, **7**, 080901.
 - 17 M. J. Fang, C. W. Tsao and Y. J. Hsu, Semiconductor nanoheterostructures for photoconversion applications, *J. Phys. D: Appl. Phys.*, 2020, **53**(14), 143001.
 - 18 K. A. Tsai and Y. J. Hsu, Graphene quantum dots mediated charge transfer of CdSe nanocrystals for enhancing photoelectrochemical hydrogen production, *Appl. Catal., B*, 2015, **164**, 271–278.
 - 19 M. Y. Chena and Y. J. Hsu, Type-II nanorod heterostructure formation through one-step cation exchange, *Nanoscale*, 2013, **5**, 363–368.
 - 20 Y. F. Lin and Y. J. Hsu, Interfacial charge carrier dynamics of type-II semiconductor nanoheterostructures, *Appl. Catal., B*, 2013, **130–131**, 93–98.
 - 21 Y. C. Chen, Y. C. Pu and Y. J. Hsu, Interfacial Charge Carrier Dynamics of the three-component In₂O₃-TiO₂-Pt heterojunction system, *J. Phys. Chem. C*, 2012, **116**, 2967–2975.
 - 22 S. Saha, N. Chaudhary, H. Mittal, G. Gupta and M. Khanuja, Inorganic-organic nanohybrid of MoS₂-PANI for advanced photocatalytic application, *Int. Nano Lett.*, 2019, **9**(2), 127–139.
 - 23 R. Sharma, M. Khanuja, S. S. Islam, U. Singhal and A. Varma, Aspect-ratio-dependent photoinduced antimicrobial and photocatalytic organic pollutant degradation efficiency of ZnO nanorods, *Res. Chem. Intermed.*, 2017, **43**(10), 5345–5364.
 - 24 T. K. Sen and S. Dawood, Review on Dye Removal from Its Aqueous Solution into Alternative Cost-Effective and Non-Conventional Adsorbents, *J. Chem. Process Eng. Res.*, 2013, **1**(104), 1–11.
 - 25 H. Mittal, A. Kumar and M. Khanuja, In-situ oxidative polymerization of aniline on hydrothermally synthesized MoSe₂ for enhanced photocatalytic degradation of organic dyes, *J. Saudi Chem. Soc.*, 2019, **23**(7), 836–845.
 - 26 N. P. Raval, P. U. Shah and N. K. Shah, Malachite green 'a cationic dye' and its removal from aqueous solution by adsorption, *Appl. Water Sci.*, 2017, **7**(7), 3407–3445.
 - 27 D. R. Doerge, M. I. Churchwell, T. A. Gehring, Y. M. Pu and S. M. Plakas, Analysis of malachite green and metabolites in fish using liquid chromatography atmospheric pressure chemical ionization mass spectrometry, *Rapid Commun. Mass Spectrom.*, 1998, **12**(21), 1625–1634.
 - 28 H. Wang, X. Yuan, Y. Wu, G. Zeng, X. Chen, L. Leng, Z. Wu, L. Jiang and H. Li, Facile synthesis of amino-functionalized titanium metal-organic frameworks and their superior visible-light photocatalytic activity for Cr(vi) reduction, *J. Hazard. Mater.*, 2015, **286**, 187–194.
 - 29 M. A. Barakat, New trends in removing heavy metals from industrial wastewater, *Arabian J. Chem.*, 2011, **4**(4), 361–377.
 - 30 A. C. Sophia, D. Catherine and V. M. Bhalambaal, Utilization of rice-husk and coconut shell carbons for water disinfection, *J. Environ. Sci. Eng.*, 2013, **55**(1), 9–16.
 - 31 S. Singh, R. Sharma and M. Khanuja, A review and recent developments on strategies to improve the photocatalytic elimination of organic dye pollutants by BiOX (X = Cl, Br, I, F) nanostructures, *Korean J. Chem. Eng.*, 2018, **35**(10), 1955–1968.
 - 32 X. Li, J. Xie, C. Jiang, J. Yu and P. Zhang, Review on design and evaluation of environmental photocatalysts, *Front. Environ. Sci. Eng.*, 2018, **12**(5), 1–32.
 - 33 Y. Yang, C. Zhang, C. Lai, G. Zeng, D. Huang, M. Cheng, J. Wang, F. Chen, C. Zhou and W. Xiong, BiOX (X = Cl, Br, I) photocatalytic nanomaterials: applications for fuels and environmental management, *Adv. Colloid Interface Sci.*, 2018, **254**, 76–93.
 - 34 M. Sun, Q. Zhao, C. Du and Z. Liu, Enhanced visible-light photocatalytic activity in BiOCl/SnO₂: heterojunction of two wide band-gap semiconductors, *RSC Adv.*, 2015, **5**(29), 22740–22752.
 - 35 M. A. Gondal, C. Xiaofeng, and M. A. Dastageer, *Novel Bismuth-Oxyhalide-Based Materials and their Applications*, Springer India, Dharan, Saudi Arabia, 1st edn, 2017, vol. 76.
 - 36 J. Jiang, K. Zhao, X. Xiao and L. Zhang, Synthesis and facet-dependent photoreactivity of BiOCl single-crystalline nanosheets, *J. Am. Chem. Soc.*, 2012, **134**(10), 4473–4476.



- 37 H. Gnyam and Y. Sasson, Hierarchical nanostructured 3D flowerlike $\text{BiOCl}_x\text{Br}_{1-x}$ semiconductors with exceptional visible light photocatalytic activity, *ACS Catal.*, 2013, **3**(2), 186–191.
- 38 G. Li, B. Jiang, S. Xiao, Z. Lian, D. Zhang, J. C. Yu and H. Li, An efficient dye-sensitized BiOCl photocatalyst for air and water purification under visible light irradiation, *Environ. Sci.: Processes Impacts*, 2014, **16**(8), 1975–1980.
- 39 S. Weng, B. Chen, L. Xie, Z. Zheng and P. Liu, Facile *in situ* synthesis of a Bi/BiOCl nanocomposite with high photocatalytic activity, *J. Mater. Chem. A*, 2013, **1**(9), 3068–3075.
- 40 B. Pare, B. Sarwan and S. B. Jonnalagadda, Photocatalytic mineralization study of malachite green on the surface of Mn-doped BiOCl activated by visible light under ambient condition, *Appl. Surf. Sci.*, 2011, **258**(1), 247–253.
- 41 N. Tahmasebi, Z. Maleki and P. Farahnak, Enhanced photocatalytic activities of $\text{Bi}_2\text{WO}_6/\text{BiOCl}$ composite synthesized by one-step hydrothermal method with the assistance of HCl, *Mater. Sci. Semicond. Process.*, 2019, **89**, 32–40.
- 42 F. Li, Y. Li, M. Chai, B. Li, Y. Hao, X. Wang and R. Liu, One-step construction of {001} facets-exposed BiOCl hybridized with Al_2O_3 for enhanced molecular oxygen activation, *Catal. Sci. Technol.*, 2016, **6**(22), 7985–7995.
- 43 Y. Shi, X. Xiong, S. Ding, X. Liu, Q. Jiang and J. Hu, *In situ* topotactic synthesis and photocatalytic activity of plate-like BiOCl/2D networks Bi_2S_3 heterostructures, *Appl. Catal., B*, 2018, **220**, 570–580.
- 44 K. Wang, C. Shao, X. Li, X. Zhang, N. Lu, F. Miao and Y. Liu, Hierarchical heterostructures of p-type BiOCl nanosheets on electrospun n-type TiO_2 nanofibers with enhanced photocatalytic activity, *Catal. Commun.*, 2015, **67**, 6–10.
- 45 Q. Li, X. Zhao, J. Yang, C. J. Jia, Z. Jin and W. Fan, Exploring the effects of nanocrystal facet orientations in g- $\text{C}_3\text{N}_4/\text{BiOCl}$ heterostructures on photocatalytic performance, *Nanoscale*, 2015, **7**(45), 18971–18983.
- 46 F. Dong, Y. Sun, M. Fu, Z. Wu and S. C. Lee, Room temperature synthesis and highly enhanced visible-light photocatalytic activity of porous BiOI/BiOCl composites nanoplates micro flowers, *J. Hazard. Mater.*, 2012, **219–220**, 26–34.
- 47 B. Liu, W. Xu, T. Sun, M. Chen, L. Tian and J. Wang, Efficient visible-light photocatalytic activity of CdS on (001) facets exposed to BiOCl, *New J. Chem.*, 2014, **38**(6), 2273–2277.
- 48 S. Shamaila, A. K. L. Sajjad, F. Chen and J. Zhang, WO_3/BiOCl , a novel heterojunction as a visible light photocatalyst, *J. Colloid Interface Sci.*, 2011, **356**(2), 465–472.
- 49 P. Xiao, J. Lou, H. Zhang, W. Song, X. L. Wu, H. Lin, J. Chen, S. Liu and X. Wang, Enhanced visible-light-driven photocatalysis from WS_2 quantum dots coupled to BiOCl nanosheets: Synergistic effect and mechanism insight, *Catal. Sci. Technol.*, 2018, **8**(1), 201–209.
- 50 N. Chaudhary and M. Khanuja, Architectural design of photodetector based on 2D(MoS_2 nanosheets)/1D(WS_2 nanorods) heterostructure synthesized by facile hydrothermal method, *J. Electrochem. Soc.*, 2019, **166**(14), 1–11.
- 51 W. Ashraf, T. Fatima, K. Srivastava and M. Khanuja, Superior photocatalytic activity of tungsten disulfide nanostructures: role of morphology and defects, *Appl. Nanosci.*, 2019, **9**(7), 1515–1529.
- 52 Y. Lei, G. Wang, S. Song and H. Zhang, Synthesis, characterization, and assembly of BiOCl nanostructure and their photocatalytic properties, *CrystEngComm*, 2009, **11**(9), 1857–1862.
- 53 J. Chen, M. Guan, W. Cai, J. Guo, C. Xiao and G. Zhang, The dominant (001) facet-dependent enhanced visible-light photoactivity of ultrathin BiOBr nanosheets, *Phys. Chem. Chem. Phys.*, 2014, **16**(38), 20909–20914.
- 54 Z. Jia, W. Chen, T. Liu, T. Huang and X. Liu, Biomolecule-assisted solvothermal synthesis and enhanced visible-light photocatalytic performance of $\text{Bi}_2\text{S}_3/\text{BiOCl}$ composites, *J. Wuhan Univ. Technol., Mater. Sci. Ed.*, 2016, **31**(4), 765–772.
- 55 J. Di, J. Xia, M. Ji, L. Xu, S. Yin, Q. Zhang, Z. Chen and H. Li, Carbon quantum dots *in situ* coupling to bismuth oxyiodide *via* reactable ionic liquid with enhanced photocatalytic molecular oxygen activation performance, *Carbon*, 2016, **98**, 613–623.
- 56 C. Tan, G. Zhu, M. Hojamberdiev, K. Okada, J. Liang, X. Luo, P. Liu and Y. Liu, Co_3O_4 nanoparticles-loaded BiOCl nanoplates with the dominant {001} facets: efficient photodegradation of organic dyes under visible light, *Appl. Catal., B*, 2014, **152–153**(1), 425–436.
- 57 L. Shan, J. Bi and Y. Liu, Roles of BiOCl (001) in face-to-faced BiOI(010)/BiOCl(001) heterojunction, *J. Nanopart. Res.*, 2018, **20**, 170.
- 58 J. Xia, L. Xu, J. Zhang, S. Yin, H. Li, H. Xu and J. Dia, Improved visible-light photocatalytic properties of Fe/BiOCl microspheres synthesized *via* self-doped reactable ionic liquids, *CrystEngComm*, 2013, **15**(46), 10132–10141.
- 59 S. Singh, A. Ruhela, S. Rani, M. Khanuja and R. Sharma, Concentration specific and tunable photoresponse of bismuth vanadate functionalized hexagonal ZnO nanocrystals based photoanodes for photoelectrochemical application, *Solid State Sci.*, 2018, **76**, 48–56.
- 60 S. Ebraheem and A. El-Saied, Bandgap determination from diffuse reflectance measurements of irradiated lead borate glass system doped with TiO_2 by using diffuse reflectance technique, *Mater. Sci. Appl.*, 2013, **4**(5), 324–329.
- 61 F. Li, Y. Li, M. Chai, B. Li, Y. Hao, X. Wang and R. Liu, One-step construction of {001} facet-exposed BiOCl hybridized with Al_2O_3 for enhanced molecular oxygen activation, *Catal. Sci. Technol.*, 2016, **6**(22), 7985–7995.
- 62 H. Zhang, R. Zong and Y. Zhu, Photocorrosion inhibition and photoactivity enhancement for zinc oxide *via* hybridization with monolayer polyaniline, *J. Phys. Chem. C*, 2009, **113**(11), 4605–4611.
- 63 B. Sarwan, A. D. Acharya and B. Pare, Visible light-driven photocatalytic degradation and mineralization of the malachite green dye in a slurry photoreactor, *Part. Sci. Technol.*, 2017, **35**(4), 472–478.



- 64 X. Han, S. Dong, C. Yu, Y. Wang, K. Yang and J. Sun, Controllable synthesis of Sn-doped BiOCl for efficient photocatalytic degradation of mixed-dye wastewater under natural sunlight irradiation, *J. Alloys Compd.*, 2016, **685**, 997–1007.
- 65 Z. Shen, Q. Han, W. Liu, X. Wang and J. Zhu, One-step synthesis of Bi(Bi₂S₃)/BiOCl heterojunctions by a simple solid-state milling method and their visible light photoreactivity, *J. Mater. Sci.*, 2019, **54**(1), 613–624.
- 66 X. Jia, Q. Han, X. Wang and J. Zhu, Milling-induced synthesis of BiOCl_{1-x}Br_x solid solution and their adsorptive and photocatalytic performance, *Photochem. Photobiol.*, 2018, **94**(5), 942–954.
- 67 K. Li, Y. Liang, J. Yang, H. Zhang, G. Yang and W. Lei, BiOCl/Fe₂O₃ heterojunction nanoplates with the enhanced visible-light-driven photocatalytic performance for degrading organic pollutants and reducing Cr(vi), *J. Photochem. Photobiol., A*, 2018, **364**, 240–249.
- 68 Y. Peng, Y. G. Mao, P. F. Kan, J. Y. Liu and Z. Fang, Controllable synthesis and photoreduction performance towards Cr(vi) of BiOCl micro rods with exposed (110) crystal facets, *New J. Chem.*, 2018, **42**(20), 16911–16918.
- 69 H. Xu, Z. Wu, M. Ding and X. Gao, Microwave-assisted synthesis of flower-like BN/BiOCl composites for photocatalytic Cr(vi) reduction upon visible-light irradiation, *Mater. Des.*, 2017, **114**, 129–138.
- 70 H. Li and L. Zhang, Oxygen vacancy induced selective silver deposition on the {001} facets of BiOCl single-crystalline nanosheets for enhanced Cr(vi) and sodium pentachlorophenol removal under visible light, *Nanoscale*, 2014, **6**(14), 7805–7810.
- 71 R. Arasteh, M. Masoumi, A. M. Rashidi, L. Moradi, V. Samimi and S. T. Mostafavi, Adsorption of 2-nitrophenol by multi-wall carbon nanotubes from aqueous solutions, *Appl. Surf. Sci.*, 2010, **256**(14), 4447–4455.
- 72 X. V. Doorslaer, P. M. Heynderickx, K. Demeestere, K. Debevere, H. V. Langenhove and J. Dewulf, TiO₂ mediated heterogeneous photocatalytic degradation of moxifloxacin: operational variables and scavenger study, *Appl. Catal., B*, 2012, **111–112**, 150–156.
- 73 J. T. Kirner and R. G. Finke, Water-oxidation photoanodes using organic light-harvesting materials: a review, *J. Mater. Chem. A*, 2017, **5**, 19560–19592.

